

Terahertz Depolarization Effects in Colloidal TiO₂ Films Reveal Particle Morphology

Søren A. Jensen,^{†,‡} Klaas-Jan Tielrooij,[¶] Euan Hendry,[§] Mischa Bonn,^{*,‡} Ivan Rychetský,^{||} and Hynek Němec^{||}

[†]FOM Institute for Atomic and Molecular Physics, Science Park 104, 1098 XG Amsterdam, The Netherlands

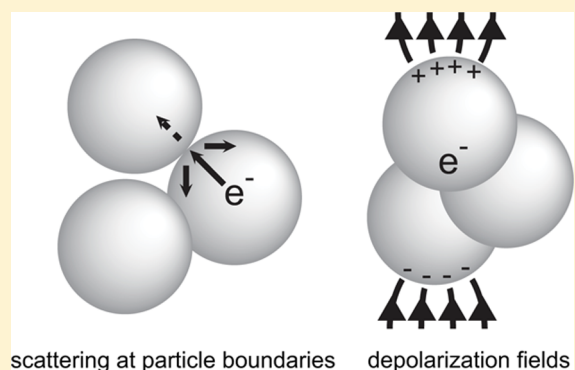
[‡]Max Planck Institute for Polymer Research, Ackermannweg 10, 55128 Mainz, Germany

[¶]ICFO—The Institute of Photonic Sciences, Mediterranean Technology Park, Castelldefels, Barcelona, Spain

[§]School of Physics, University of Exeter, Stocker Road, Exeter EX4 4QL, United Kingdom

^{||}Institute of Physics, Academy of Sciences of the Czech Republic, Na Slovance 2, 182 21 Prague, Czech Republic

ABSTRACT: Films of colloidal TiO₂ nanoparticles are widely used in photovoltaic and photocatalytic applications, and the nature of electrical conductivity in such materials is therefore of both fundamental and practical interest. The conductive properties of colloid TiO₂ films depend strongly on their morphology and deviate greatly from the properties of the bulk material. We report ultrafast photoconductivity studies of films consisting of sintered TiO₂ particles of very different sizes performed using time-resolved terahertz spectroscopy. Remarkably, identical photoconductivity spectra are observed for films of particles with diameters of tens and hundreds of nanometers, respectively. The independence of photoconductivity on particle size directly demonstrates that the terahertz photoconductive response of colloidal TiO₂ films is not affected by carrier back-scattering at particle boundaries as has previously been concluded, but rather by depolarization fields resulting from the spatial inhomogeneities in the dielectric function inherent to these types of films. Modeling of the influence of depolarization fields on the terahertz conductivity allows us to explain the measured data and gain insights into the morphology of the film. Specifically, we show that the observed photoconductivity spectra reflect percolated pathways in the colloidal TiO₂ nanoparticles films, through which charge carrier diffusion can occur over macroscopic length scales.



■ INTRODUCTION

Titanium dioxide (TiO₂) is a wide bandgap semiconductor commonly used in photocatalysis^{1,2} for instance, for the photosplitting of water³ and in photovoltaics,^{4,5} where it can be sensitized by optically active molecular dyes^{6,7} (benefiting from fast dye to oxide electron injection rates⁸) or semiconductor quantum dots.^{9,10} Porous films with a large surface area made from TiO₂ nanoparticles are often employed for these purposes, and the electronic transport properties of such films are therefore of great importance. Despite their technological importance, the electron transport mechanisms in films composed of connected particles have remained poorly understood. For example, the room temperature dc mobility in porous TiO₂ ($\sim 7 \times 10^{-6}$ cm²/(V s))¹¹ is many orders of magnitude smaller than the intrinsic mobility of the bulk material (~ 1 cm²/(V s)).¹² Since the dc conductivity is inherently related to long-range charge transport, it does not reveal transport mechanisms on shorter (nanoscale) distances, which represent the intrinsic limit for long-range transport. Although it is now possible to characterize the conductivity of individual nanoobjects,¹³ it is still challenging to characterize

the conductive coupling between the nanoobjects and the effect of the morphology of the large ensembles of nanoparticles forming colloidal films.

To investigate the interplay between the intrinsic conducting properties of the bulk TiO₂ material and the morphology of particle films, we employ time-resolved terahertz (THz) spectroscopy.^{14,15} Here charge carriers are optically excited and probed by a freely propagating oscillating electric field. The mobility of photogenerated charges can thus be probed in a noncontact fashion over nanometer distances and with sub-picosecond time resolution so that the carriers are probed before they reach an equilibrium with defect trapping states.⁵

We investigate two colloidal TiO₂ films composed of submicrometer-sized (150–250 nm), and nanometer-sized (15–20 nm) particles, respectively. Measuring the THz photoconductivity with two significantly different particle sizes allows us to draw conclusions about the relation between

the effective response of the particle film and the intrinsic photoconductivity of the particles. In bulk TiO₂ the photoconductivity follows the predictions of the common Drude model for free charges undergoing momentum randomizing scattering.¹² To describe the strongly non-Drude response observed in nanoparticle films, preferential carrier backscattering at grain boundaries has frequently been included via the modified Drude–Smith (DS) model.^{16–18} The drawback of this model is that it does not respect time homogeneity since it assumes that the first scattering event is different from the subsequent ones. Moreover, the DS model is purely phenomenological, and does not reflect, for example, the characteristic dimensions of the particles. Improved modeling was recently achieved using Monte-Carlo calculations of the conductivity of semiconducting nanoparticles, taking into account the carrier mean free path and dimensions of the particles.¹⁹ In TiO₂, however, the relatively small room temperature charge carrier mean free path (~ 1 nm)²⁰ suggests that only a small fraction of the total carrier scattering events will occur from surfaces, even for films of nanoparticles.¹⁹

This calls for an alternative explanation for the significantly different conductivities observed in bulk and porous TiO₂: the effect of depolarization fields. It has been shown²⁰ that the applied THz probe field is screened by photoinduced free carriers inducing dipoles in the highly polarizable TiO₂ particles. This leads to a nontrivial relationship between the measured macroscopic conductivity and the intrinsic conductivity of charge carriers in the particles, as the level of field screening depends on both probe frequency and photoinduced conductivity through the change in permittivity, as well as the film morphology. Note that the influence of local fields is a purely electromagnetic effect which acts in addition to potential preferential backscattering of charge carriers, if present.⁵ We note that the plasmon model presented in ref 21 is largely equivalent to the concept of depolarization fields described by the effective medium theory. Both approaches essentially describe the response of an inhomogeneous system to an applied electric field oscillating at high frequencies. We do not apply the plasmon model here since it would be very difficult to accurately determine the frequencies, lifetimes, and oscillator strengths of the plasmon modes in the complex geometries under study.

The applicability of the alternative models is under debate: Both carrier backscattering and depolarization fields have previously been employed to explain results from various films of TiO₂ nanoparticles.^{17,19,20}

Here we demonstrate experimentally, using different samples, that the characteristic photoconductive response is caused by depolarization fields rather than scattering at particle boundaries. We compare our data with a model based on the effective medium theory and finite-element calculations to determine the effective response of relevant model structures. The comparison between numerical modeling and measured spectra confirms that depolarization fields are the cause of the observed response and allows us to conclude that the TiO₂ films studied have rather complex percolation pathways, responsible for long-range charge transport within the films.

MATERIALS AND METHODS

Samples. Two different films made from different commercial pastes of TiO₂ particles were investigated. One was prepared from the Solaronix Ti-Nanoxide T paste which contains particles with diameter 15–20 nm (referred to as

nanoparticles), the other was prepared from Dyesol TiO₂ paste WER2-O with particle sizes in the range 150–250 nm (referred to as microparticles). The pastes were doctorbladed onto a sandblasted fused silica substrate, dried for 30 min at 115 °C, and finally sintered for 1 h at 500 °C. SEM images of the films are shown in Figure 1a. Both films consist of the anatase crystal form as confirmed by Raman spectroscopy.

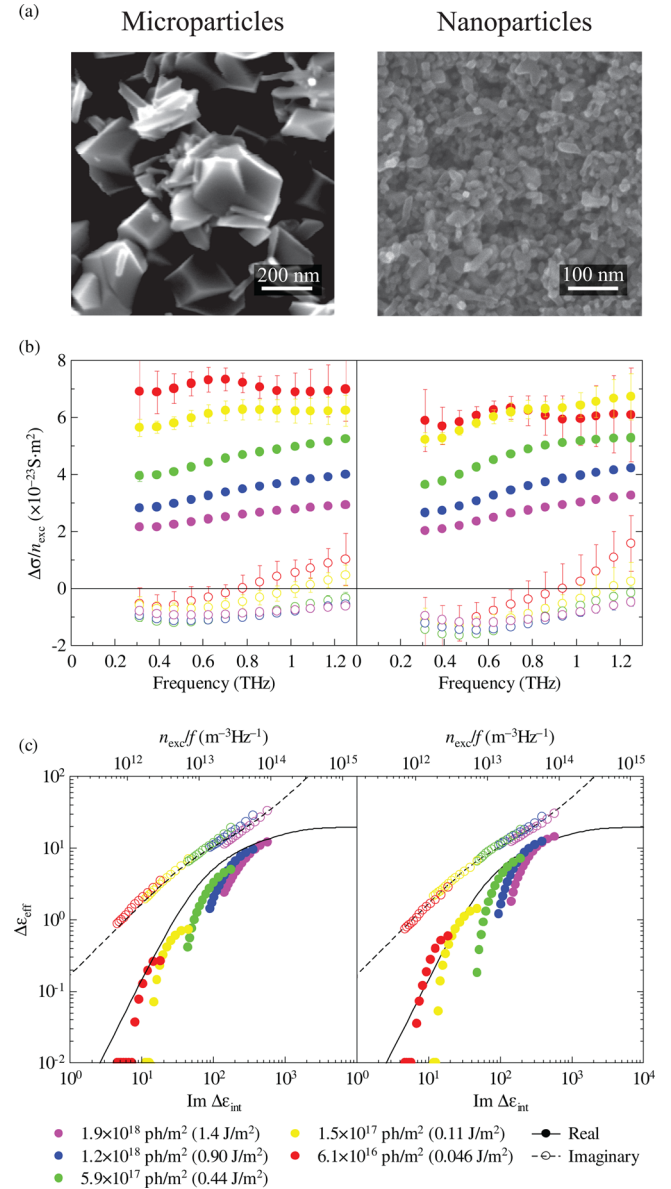


Figure 1. (a) SEM images of the TiO₂ films, notice the different scale bars. (b) Frequency-dependent effective photoconductivity normalized by the photon density recorded at a pump–probe delay of 4 ps in the microparticle (left) film and the nanoparticle film (right) at a number of photon fluxes. Filled symbols show the real part, and open symbols show the imaginary part. Error bars show the standard deviation obtained from multiple consecutive scans of the transmitted THz waveform. (c) Effective transient permittivity $\Delta\epsilon_{\text{eff}}$ for nanoparticles and microparticles calculated from the conductivity data, as a function of inverse probe frequency times photon density. Lines in panels c show the calculated effective response of the structure in Figure 3c plotted versus the imaginary part of the intrinsic transient permittivity $\Delta\epsilon_{\text{int}}$.

Time Resolved THz Spectroscopy. The setup employed for time-resolved THz spectroscopy (similar to that in ref 22) was driven by an amplified Ti:sapphire laser system that delivers 800 nm, 100 fs pulses at 3 W of output power and a repetition rate of 1 kHz. Probe pulses consisting of frequencies in the 0.3–1.3 THz range were generated by focusing 50 mW of this power onto a 1 mm thick ZnTe crystal.¹⁴ Light pulses of 266 nm wavelength were generated by sum frequency mixing of fundamental 800 nm pulses and 400 nm pulses obtained by frequency doubling. The pump spot size was enlarged by a diverging lens to a diameter larger than 1 cm, ensuring a homogeneous photoexcitation over the entire probed area (the THz probe was focused to a spot smaller than 1 mm). Excitation densities were estimated from the transmission through a series of calibrated pinholes positioned at the sample position (THz focus). As anatase TiO₂ has a bandgap of ~3.3 eV,¹ charge carriers can be directly excited by 266 nm (4.66 eV) pulses.

In a pump–probe experiment, the excitation pulse induces a change in the effective permittivity of the sample $\Delta\epsilon_{\text{eff}}(\omega) = i\Delta\sigma_{\text{eff}}(\omega)/(\omega\epsilon_0)$ (where $\Delta\sigma_{\text{eff}}$ is the effective photoinduced conductivity, ϵ_0 is the vacuum permittivity, and ω is the angular frequency of the probe field) which leads to a change in the field strength of the transmitted probe pulse $\Delta T(\omega)$. Provided that the photoinduced change is weak and the thickness of the photoexcited region l is small compared to the probe wavelength, the transient photoconductivity can be retrieved from the frequency-dependent transmitted THz waveforms using^{21,23}

$$\Delta\sigma_{\text{eff}}(\omega) = -\frac{\epsilon_0 c(1+n)}{l} \frac{\Delta T(\omega)}{T(\omega)} \quad (1)$$

where $T(\omega)$ is the transmitted probe field through the unexcited sample, c is the speed of light, and n is the refractive index of the substrate (in our case the unexcited film). This expression is valid when the transient conductivity $\Delta\sigma_{\text{eff}}$ varies on a time scale much longer than the THz pulse length, that is, when the leading edge of the THz pulse probes the same dielectric function as the trailing edge.²⁴ The region photoexcited by 266 nm light in TiO₂ has an exponential profile with a characteristic penetration depth of about 20 nm for bulk TiO₂²⁵ and ~70 nm for colloid films.²⁰ Nevertheless, it was shown in ref 23 that eq 1 is valid for an exponential profile of the transient conductivity, only l is replaced with the linear absorption depth.

Numerical Simulations. The effective permittivity response of the model structures in Figure 3 was calculated using FreeFem++, which is a programming language and software focused on solving partial differential equations using the finite element method.²⁶ At first, by means of a convenient image processing procedure, the 2D structures were approximated by unstructured triangular meshes.²⁷ Then the electric field in the sample was calculated by solving quasi-static Maxwell equations with boundary conditions guaranteeing an electric field along the film. Finally, the calculated distribution of energy density was averaged over the whole sample and equated to the energy density of an equivalent homogeneous film

$$\frac{1}{2}V^{-1} \int_V \epsilon_{\text{int}}(\mathbf{r}) \mathbf{E}^2(\mathbf{r}) dV = \frac{1}{2} \mathbf{D} \cdot \mathbf{E} = \frac{1}{2} \epsilon_{\text{eff}} \mathbf{E}^2 \quad (2)$$

which defines the effective permittivity ϵ_{eff} . Here $\epsilon_{\text{int}}(\mathbf{r})$ and $\mathbf{E}(\mathbf{r})$ are local permittivity and electric field, respectively; \mathbf{E} and

\mathbf{D} are the volume average of electric field and displacement, respectively ($\mathbf{E} = V^{-1} \int_V \mathbf{E}(\mathbf{r}) dV$).

The quasi-static approximation is applicable when the dimensions D of the constituting particles are much smaller than the probing wavelength in the constituents; that is, $D \ll \lambda/(\epsilon_{\text{int}})^{1/2}$. Within this approximation, the effective response depends solely on the morphology of the structure, whereas it is independent of the actual scale of the structure.

The ground-state microscopic permittivities (without photoexcitation) employed in the calculations were 35 for the particles and 1 for the air in which the particles are dispersed. The graphs in Figure 3 were calculated for purely imaginary $\Delta\epsilon_{\text{int}}$ which corresponds to a purely conductive transient intrinsic response ($\text{Im}\Delta\sigma_{\text{int}} = 0$). The results will be discussed later in detail; a partial understanding can be gained based on section 3 in ref 5.

■ RESULTS AND DISCUSSION

Transient Conductivity. Figure 1b shows the THz frequency-resolved complex photoconductivity for the microparticle film and the nanoparticle film, respectively, measured 4 ps after photoexcitation. In agreement with previous works,^{17,19,20} we find that the effective photoconductive response of nanoporous TiO₂ films qualitatively differs from bulk in that the transient conductivity exhibits a real component which increases with increasing frequency and a negative imaginary component. The nature of these features, and thus how to relate the effective photoresponse to the intrinsic response of the particles is still a subject of debate.^{5,14}

At this point we can, without further analysis, with certainty exclude backscattering at the particle boundaries as the main source of the shape of the conductivity spectra: The spectra of transient conductivities $\Delta\sigma_{\text{eff}}(\omega)$ are almost identical for films of nanoparticles and films of microparticles, whereas boundary effects would lead to considerably different conductivity spectra in particles with different sizes.¹⁹ This finding is also consistent with the fact that the carrier mean free path is much smaller than the particle radii for both films as mentioned above.

Further, a distinct change in the frequency dependence of the conductivity as the photon flux is increased is evident from Figure 1b. This is particularly noticeable in the imaginary component of the conductivity, which is positive at high frequencies for low excitation powers, but negative over the entire probe spectrum for the highest excitation powers. Note that the employed excitation powers are not high enough to induce significant carrier–carrier scattering.²⁸ At this point it is also important to note that most linear models that describe the effects of backscattering on microscopic conductivity, such as the DS¹⁶ and the numerical Monte-Carlo simulations presented in ref 19 exhibit conductivities that simply scale with carrier density. This is in contrast to our findings. These considerations provide clear evidence that the observed intensity dependence is caused by depolarization fields, which are carrier density dependent.²⁰

We also measured the magnitude of the pump induced THz absorption $|\Delta T/T|$ versus pump delay for both microparticles and nanoparticles for a number of fluences. Figure 2 shows the data measured at the same pump intensity for both samples; a very similar behavior is observed, consistent with the conductivity data shown in Figure 1. The measurements performed at other pump intensities showed the same dynamics when normalized to the peak amplitude.

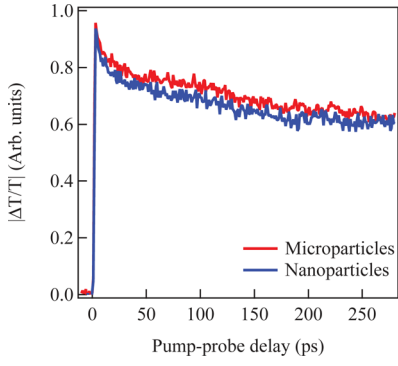


Figure 2. Pump-induced THz absorption vs pump-probe delay for microparticles and nanoparticles, both excited by a photon density of 1.9×10^{18} ph/m² (1.4 J/m²). Exciting with other pump intensities gave the same dynamics.

Below we introduce a numerical model that accounts for the effects of depolarization fields. We show that by comparing the effective photoinduced permittivity changes ($\Delta\epsilon_{\text{eff}}$) measured in our THz experiments to predictions from the model, one can gain insight into the microscopic morphology of the films.

Effective Medium and Transient Permittivity. Since we deal with particles much smaller than the probing wavelength, we account for the depolarization fields via the effective medium theory. Here the permittivity change in the composite film consisting of oxide particles, and the surrounding medium is described by a single effective permittivity ϵ_{eff} which is experimentally accessible. ϵ_{eff} is related to the intrinsic permittivity ϵ_{int} of the TiO₂ particles through the morphology of the film, and the relationship can be evaluated analytically only in very specific cases: for example, the Maxwell-Garnett model well describes sparse spherical particles separated in a non-conducting matrix²⁹ and has successfully been applied to monitor the phase transition from semiconducting to metallic

in bulk VO₂.³⁰ Numerical calculations are generally required to characterize more complex morphologies.

In many situations, we are asking the inverse question: can we gain information on the morphology from the measured response? This question can be addressed when it is possible to measure the effective permittivity ϵ_{eff} as a function of the intrinsic particle permittivity ϵ_{int} , since the morphology uniquely defines the mapping $\epsilon_{\text{int}} \rightarrow \epsilon_{\text{eff}}$.

Here we take advantage of the possibility to control the transient intrinsic photoconductivity $\Delta\sigma_{\text{int}}$ by varying the excitation photon density. In ref 5 it was shown that the effective conductivity $\Delta\sigma_{\text{eff}}$ should exhibit a different dependence on the photon density for percolated and nonpercolated systems. We will show that even more detailed insight can be gained from such a dependence.

A total intrinsic permittivity $\epsilon_{\text{int}} = \epsilon_{\text{int},0} + \Delta\epsilon_{\text{int}}$ (where $\epsilon_{\text{int},0}$ is the permittivity of the unexcited material and $\Delta\epsilon_{\text{int}} = i\Delta\sigma_{\text{int}}/(\omega\epsilon_0)$ is the transient permittivity induced by the photo-excitation) leads to an effective permittivity $\epsilon_{\text{eff}} = \epsilon_{\text{eff},0} + \Delta\epsilon_{\text{eff}}$ where $\epsilon_{\text{eff},0}$ is the permittivity of the unexcited film and $\Delta\epsilon_{\text{eff}} = i\Delta\sigma_{\text{eff}}/(\omega\epsilon_0)$ is the transient effective permittivity. For bulk TiO₂ at room temperature, the intrinsic transient conductivity follows the Drude model with a very short scattering time,¹² which can be very well approximated by a real frequency-independent value $\Delta\sigma_{\text{int}} \approx n_{\text{exc}}e\mu$, where n_{exc} is the excitation density, e is the elemental charge, and μ is the electron mobility in TiO₂. Accordingly, the transient intrinsic permittivity

$$\Delta\epsilon_{\text{int}} = in_{\text{exc}}e\mu/(\omega\epsilon_0) \quad (3)$$

of TiO₂ is purely imaginary, and is controlled solely by the ratio n_{exc}/ω . In other words, if we simultaneously increase the excitation photon density and the frequency, $\Delta\epsilon_{\text{int}}$ should remain the same, and consequently the same transient effective permittivity, $\Delta\epsilon_{\text{eff}}$ should be observed. To verify this prediction we replot in Figure 1c the measured THz photoresponse data

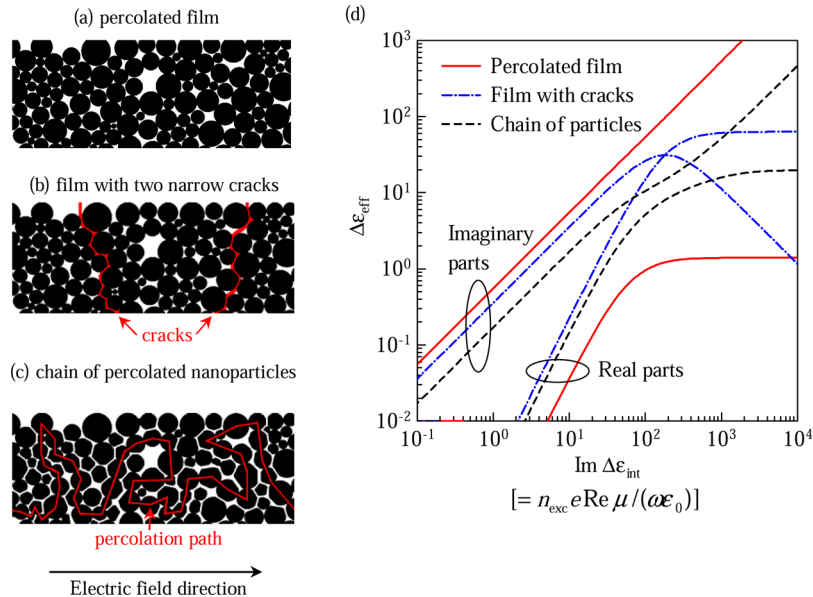


Figure 3. Calculation of the effective response of 2-dimensional model geometries. (a) The particles form a percolated film. (b) Two cracks are introduced (marked in red) so that the film is not percolated along the direction parallel to the electric field. (c) The geometry is characterized by a complex percolation path (highlighted by a red line). The filling factors are 0.845, 0.841, and 0.798 for structures a, b, and c, respectively. (d) Complex effective transient permittivity $\Delta\epsilon_{\text{eff}}$ as a function of the imaginary part of the microscopic transient permittivity $\Delta\epsilon_{\text{int}}$ for the model geometries shown.

from Figure 1b expressed as $\Delta\epsilon_{\text{eff}}$ versus the ratio n_{exc}/f . Indeed, we see that the imaginary parts measured for various excitation densities overlap with each other to form a single curve. This lends further support to the conclusion that the response is primarily and predominantly determined by depolarization fields (other processes such as carrier–carrier scattering should not depend solely on the ratio n_{exc}/ω). The agreement between the data traces of the real part of $\Delta\epsilon_{\text{eff}}$ appears to be worse. While the absolute errors in the real and imaginary parts are comparable, they seem more pronounced for the real part in the log–log plot, since the real part is considerably smaller than the imaginary part. Moreover, in the Drude response we neglected the real part of $\Delta\epsilon_{\text{int}}$; its inclusion shifts the real part of $\Delta\epsilon_{\text{eff}}$ more than the imaginary part.

Numerical Modeling. To find the morphology related to the measured universal dependence $\Delta\epsilon_{\text{eff}}(\Delta\epsilon_{\text{int}})$, we evaluate $\Delta\epsilon_{\text{eff}}$ as a function of $\text{Im}\Delta\epsilon_{\text{int}}$ (neglecting the real part of $\Delta\epsilon_{\text{int}}$ following the discussion above) for various model morphologies by numerical calculations described in the Materials and Methods section. To capture the main aspects related to the degree of percolation, we investigate a 2-dimensional model structure consisting of percolated, closely packed spheres (Figure 3a). We also investigate two geometries with suppressed percolation, derived by introduction of specific defects, but possessing a similar filling factor (Figure 3b,c).

The results of the simulation are shown in Figure 3d. For low values of $\text{Im}\Delta\epsilon_{\text{int}}$ the imaginary part of the effective transient permittivity is proportional to $\text{Im}\Delta\epsilon_{\text{int}}$ for all geometries. More generally, the *complex* effective transient permittivity $\Delta\epsilon_{\text{eff}}$ is directly proportional to the *complex* transient intrinsic permittivity $\Delta\epsilon_{\text{int}}$. This behavior stems from the fact that a low transient microscopic permittivity causes only a weak perturbation to the distribution of the electric field intensity. Therefore the perturbation is linearly proportional to $\Delta\epsilon_{\text{int}}$.³¹ In turn, the effective response scales linearly with the microscopic one, independent of the degree of percolation of the structure. The real part of the transient effective permittivity is associated with second-order terms of the dependence $\Delta\epsilon_{\text{eff}}(\text{Im}\Delta\epsilon_{\text{int}})$, therefore it is much smaller in magnitude than the imaginary part, and it increases quadratically with increasing frequency (the slope of two in the log–log plot).

Higher transient intrinsic permittivities substantially modify the distribution of the electric field, and the relation $\Delta\epsilon_{\text{eff}}(\Delta\epsilon_{\text{int}})$ thus deviates from linearity and reflects the degree of percolation.

The sections i–iii below detail the findings of the simulation for the three model systems in Figure 3a–c. The major features pointed out in sections i and ii can also be derived analytically for, for example, the Maxwell–Garnett approximation.⁵

(i) For well percolated systems (analogous to Figure 3a), $\text{Im}\Delta\epsilon_{\text{eff}}$ is directly proportional to $\text{Im}\Delta\epsilon_{\text{int}}$. In many situations, the proportionality constant is almost identical to that found in the low- $\Delta\epsilon_{\text{int}}$ regime.⁵ For a purely conductive microscopic response, the effective response is also mainly conductive ($\text{Re}\Delta\epsilon_{\text{eff}} \ll \text{Im}\Delta\epsilon_{\text{eff}}$). The transient capacitive effective response ($\text{Re}\Delta\epsilon_{\text{eff}}$) is very weak as it is limited by the layout and amount of the non-photoconducting matrix, hence also its saturation for high $\text{Im}\Delta\epsilon_{\text{int}}$.

(ii) Qualitatively different behavior is observed in non-percolated systems (such as in Figure 3b). The lack of a percolated path implies that the applied electric field separates positive and negative charges at the opposite sides of the unconnected subparts. This gives rise to a restoring force and in

turn, to plasma-like oscillations.³² Their resonance frequency shifts up with increasing $\text{Im}\Delta\epsilon_{\text{int}}$ and the corresponding transient effective permittivity is inversely proportional to $\text{Im}\Delta\epsilon_{\text{int}}$ (seen as the negative slope in the log–log plot).⁵ Similarly, as in the case of the percolated geometries, there is a contribution related to the non-photoconducting component which limits the transient capacitive response and causes the saturation of $\text{Re}\Delta\epsilon_{\text{eff}}$. These properties imply that the curves for $\text{Re}\Delta\epsilon_{\text{eff}}$ and $\text{Im}\Delta\epsilon_{\text{eff}}$ intersect for a certain $\text{Im}\Delta\epsilon_{\text{int}}$.

(iii) In a physically reasonable geometry, a percolation path will either exist or not, and thus, strictly speaking, any system falls into one of the two above categories. However, if the system contains complex percolation path(s) or subpaths, there may be a broad range where the transition from the low- $\Delta\epsilon_{\text{int}}$ regime to the high- $\Delta\epsilon_{\text{int}}$ regime occurs. For example, in the case of a tangled chain (Figure 3c), the slope of $\log \text{Im}\Delta\epsilon_{\text{eff}}$ vs $\log \text{Im}\Delta\epsilon_{\text{int}}$ undergoes a substantial change, and there is a very broad range where $\text{Re}\Delta\epsilon_{\text{eff}}$ cannot be described by either limit (quadratic or saturated behavior).

The points i–iii constitute the basis for our interpretation of the measured spectra shown in Figure 1c. Since the measured transient real and imaginary effective permittivities do not tend to form a clear intersection, we conclude that a simple or complex percolation path must exist. It is also evident that the dependence $\text{Im}\Delta\epsilon_{\text{eff}}(\text{Im}\Delta\epsilon_{\text{int}})$ is not linear, and that the real and imaginary transient effective permittivities approach each other, which implies that even the model of a strongly percolated film is rather far from reality. This means that the particles in the investigated films form rather complex percolation paths. The calculated response of the complex percolated film shown in Figure 3c is plotted together with the measured data in Figure 1c.

The comparison of the data with the simulation allows us to obtain an estimate of the THz mobility of anatase TiO_2 particles from their microscopic transient permittivity $\Delta\epsilon_{\text{int}}$ which is proportional to the mobility (see eq 3). We estimate the intrinsic mobility in such a way to obtain a good match with the calculated dependence $\Delta\epsilon_{\text{eff}}(\Delta\epsilon_{\text{int}})$. The estimated value of $20 \text{ cm}^2 \text{ V}^{-1} \text{ s}^{-1}$ is comparable to that found in a bulk rutile TiO_2 sample.¹²

Although the geometry sketched in Figure 3 c gives some idea what the real morphology of the film may look like, the main aim here is not to find a “perfect” geometry exactly matching the measured dependence $\Delta\epsilon_{\text{eff}}(\Delta\epsilon_{\text{int}})$. Instead, we would like to point out that the widely used simple effective medium approximations such as the Maxwell–Garnett, Bruggeman or brick-wall models may be insufficient to capture the real geometry of nanoparticulate or microparticulate films. The morphology of the films allows for some long-range transport, which is necessary for applications that rely on high surface to volume ratios and efficient electron harvesting, such as dye-sensitized solar cells.^{6,7}

Qualitatively similar results are also expected in 3D structures. The key factor which controls the response is the presence or absence of a percolation pathway in the direction of the probing electric field. Note that large-scale calculations would be unavoidable in order to obtain the $\epsilon_{\text{eff}}(\epsilon_{\text{int}})$ (Figure 3) in three dimensions.

The Effect of Atmospheric Water. The observation that depolarization fields dominate the effective photoresponse has interesting implications. One particular feature of depolarization effects is that they are very sensitive to the polarizability of the environment surrounding the photoconducting particles.

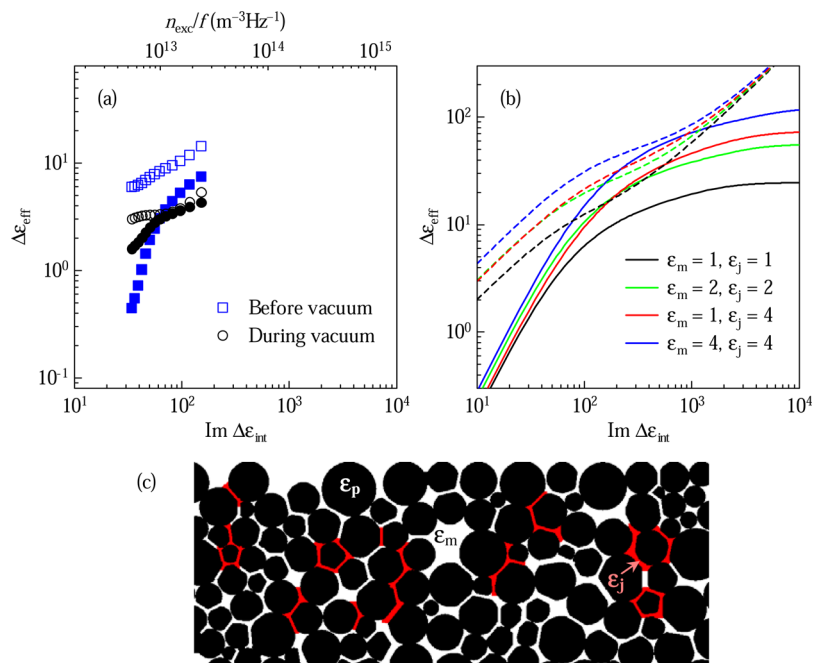


Figure 4. (a) Effective transient permittivity measured with excitation photon flux of 6.0×10^{17} ph/m^2 ($0.45 \text{ J}/\text{m}^2$) on the nanoparticle TiO_2 film in ambient air and in vacuum, plotted versus inverse probe frequency times excitation density. The bottom axis shows the corresponding change in imaginary microscopic permittivity calculated from eq 3 assuming $\mu = 20 \text{ cm}^2 \text{ V}^{-1} \text{ s}^{-1}$. (b) Real (solid lines) and imaginary (dashed lines) effective transient permittivity as function of the imaginary part of the microscopic permittivity calculated for varying degrees of water percolation. (c) Model system used for permittivity calculations, same structure as that shown in Figure 3c with permittivity of surrounding medium ϵ_m and permittivity of connecting regions ϵ_j .

Figure 4a shows the change in effective transient permittivity measured on the nanoparticle TiO_2 film upon changing the environment from ambient air to vacuum. In ambient air at room temperature, water molecules are efficiently adsorbed on TiO_2 surfaces,¹ which can be (partially) removed when going to vacuum. Since water has a larger permittivity than air, the permittivity contrast between the particles and their surroundings will be smaller. The presence of water thus leads to smaller depolarization effects and a larger effective transient permittivity. This effect was simulated by calculating the effective transient permittivity of the model system shown in Figure 3c while varying the permittivity of the surrounding matrix (ϵ_m). To simulate the effect of increased percolation we also introduced connecting regions between adjacent particles (see Figure 4c) of permittivity ϵ_j . In Figure 4b the blue curves represent the situation where the voids between the particles are completely filled with water ($\epsilon_{\text{H}_2\text{O}} \approx 4$ at 1 THz ³³), the green curves correspond to roughly 33% water filling ($\epsilon_m = 33\% \epsilon_{\text{H}_2\text{O}} + 67\% \epsilon_{\text{vac}} = 2$) distributed evenly in the pores, the red curves correspond to a small amount ($\sim 15\%$) of water concentrated at the connecting regions, and the black curves correspond to total absence of water. From the data in Figure 4b we conclude that if water is randomly distributed in the isolating matrix, an unrealistically large water content is needed to increase the effective permittivity significantly. However, the more physically relevant picture of small amounts of water concentrated at the pores between close particles can also explain the experimentally observed shift in permittivity shown in Figure 4a. Note that the real and imaginary permittivities measured in vacuum, shown in Figure 4a, do not cross, in accordance with the simulations. The simulated magnitude of $\Delta\epsilon_{\text{eff}}$ is larger than the measured data. This discrepancy can be expected as this is a simulation of one model system with a

particular morphology, and as stated above, the goal is not to find the exact morphology that reproduces the magnitudes. Similarly, even though the simulations presented above in Figure 1 were carried out without accounting for the effect of water in ambient air, the conclusions remain the same.

These observations lend further support to the conclusion that the observed non-Drude-like photoconductivity in colloidal films is related to the contrast in permittivity of particles and the surrounding environment, which controls the strength of the depolarization fields. Moreover, the sensitivity of the effective THz photoresponse to the permittivity of the environment offers possible applications in fields such as gas sensing.

CONCLUSION

We have shown that the characteristic transient THz conductivity of anatase TiO_2 nanoparticle films can be explained by depolarization fields caused by the contrast in permittivity between the conducting particles and the surrounding medium without the need of correction for preferential carrier backscattering at particle surfaces. Numerical calculations of the effective conductivity of model structures provide insight into the degree of percolation of the nanoparticle films, confirming the presence of charge carrier pathways responsible for the materials long-range conductive properties. Finally, the microscopic electron mobility in anatase TiO_2 nanoparticles was estimated to be $20 \text{ cm}^2 \text{ V}^{-1} \text{ s}^{-1}$, in agreement with bulk measurements.

AUTHOR INFORMATION

Corresponding Author

*E-mail: bonn@mpip-mainz.mpg.de Tel.: +49 (0)6131 379160. Fax: +49 (0)6131 379360.

Notes

The authors declare no competing financial interest.

ACKNOWLEDGMENTS

This work has been financially supported by the Nederlandse Organisatie voor Wetenschappelijk Onderzoek (NWO) within the research program “Stichting voor Fundamenteel Onderzoek der Materie (FOM)”. The support of the Czech Science Foundation (project 13-12386S) and Czech Ministry of Education (project COST LD1202S) is also acknowledged.

REFERENCES

- (1) Linsebigler, A. L.; Guanguan, L.; Yates, T. J. Photocatalysis on TiO₂ Surfaces: Principles, Mechanisms, and Selected Results. *Chem. Rev.* **1995**, *95*, 735–758.
- (2) Fujishima, A.; Rao, T. N.; Tryk, D. A. Titanium Dioxide Photocatalysis. *J. Photochem. Photobiol. C* **2000**, *1*, 1–21.
- (3) Ni, M.; Leung, M. K.; Leung, D. Y.; Sumathy, K. A Review and Recent Developments in Photocatalytic Water-Splitting Using TiO₂ for Hydrogen Production. *Renew. Sust. Energy Rev.* **2007**, *11*, 401–425.
- (4) Kalyanasundaram, K.; Grätzel, M. Applications of Functionalized Transition Metal Complexes in Photonic and Optoelectronic Devices. *Coord. Chem. Rev.* **1998**, *77*, 347–414.
- (5) Němec, H.; Kužel, P.; Sundström, V. Charge Transport in Nanostructured Materials for Solar Energy Conversion Studied by Time-Resolved Terahertz Spectroscopy. *J. Photochem. Photobiol. A* **2010**, *215*, 123–139.
- (6) O'Regan, B.; Grätzel, M. A low-cost, High-Efficiency Solar Cell Based on Dye-Sensitized Colloidal TiO₂ Films. *Nature* **1991**, *353*, 737–740.
- (7) Hardin, B. E.; Snaith, H. J.; McGehee, M. D. The Renaissance of Dye-Sensitized Solar Cells. *Nat. Photonics* **2012**, *6*, 162–169.
- (8) Tiwana, P.; Docampo, P.; Johnston, M. B.; Snaith, H. J.; Hertz, L. M. Electron Mobility and Injection Dynamics in Mesoporous ZnO, SnO₂, and TiO₂ Films Used in Dye-Sensitized Solar Cells. *ACS Nano* **2011**, *5*, 5158–5166.
- (9) Zaban, A.; Mic, O. I.; Gregg, B. A.; Nozik, A. J. Photosensitization of Nanoporous TiO₂ Electrodes with InP Quantum Dots. *Langmuir* **1998**, *12*, 3153–3156.
- (10) Robel, I.; Subramanian, V.; Kuno, M.; Kamat, P. V. Quantum dot Solar Cells. Harvesting Light Energy with CdSe Nanocrystals Molecularly Linked to Mesoscopic TiO₂ Films. *J. Am. Chem. Soc.* **2006**, *128*, 2385–2393.
- (11) Dittrich, T. Porus TiO₂: Electron Transport and Application to Dye Sensitized Injection Solar Cells. *Phys. Stat. Sol. (a)* **2000**, *182*, 447–455.
- (12) Hendry, E.; Wang, F.; Shan, J.; Heinz, T. F.; Bonn, M. Electron Transport in TiO₂ Probed by THz Time-Domain Spectroscopy. *Phys. Rev. B* **2004**, *69*, 081101.
- (13) Ko, T. Y.; Tsai, M.-H.; Lee, C.-S.; Sun, K. W. Electron Transport Mechanisms in Individual Cobalt-Doped ZnO Nanorods. *J. Nanopart. Res.* **2012**, *14*, 1253.
- (14) Ulbricht, R.; Hendry, E.; Shan, J.; Heinz, T. F.; Bonn, M. Carrier Dynamics in Semiconductors Studied with Time-Resolved Terahertz Spectroscopy. *Rev. Mod. Phys.* **2011**, *83*, 543–586.
- (15) Lloyd-Hughes, J.; Jeon, T.-I. A Review of the Terahertz Conductivity of Bulk and Nano-Materials. *J. Infrared, Millimeter, Terahertz Waves* **2012**, *33*, 871–925.
- (16) Smith, N. V. Classical Generalization of the Drude Formula for the Optical Conductivity. *Phys. Rev. B* **2001**, *64*, 155106.
- (17) Turner, G. M.; Beard, M. C.; Schmittenmaer, C. A. Carrier Localization and Cooling in Dye-Sensitized Nanocrystalline Titanium Dioxide. *J. Phys. Chem. B* **2002**, *106*, 11716–11719.
- (18) Cooke, D. G.; MacDonald, A. N.; Hryciw, A.; Wang, J.; Li, Q.; Meldrum, A.; Hegmann, F. A. Transient Terahertz Conductivity in Photoexcited Silicon Nanocrystal Films. *Phys. Rev. B* **2006**, *73*, 193311.

(19) Němec, H.; Kužel, P.; Sundström, V. Far-Infrared Response of Free Charge Carriers Localized in Semiconductor Nanoparticles. *Phys. Rev. B* **2009**, *79*, 115309.

(20) Hendry, E.; Koeberg, M.; O'Regan, B.; Bonn, M. Local Field Effects on Electron Transport in Nanostructured TiO₂ Revealed by Terahertz Spectroscopy. *Nano Lett.* **2006**, *6*, 755–759.

(21) Nienhuys, H.-K.; Sundström, V. Intrinsic Complications in the Analysis of Optical-Pump, Terahertz Probe Experiments. *Phys. Rev. B* **2005**, *71*, 235110.

(22) Beard, M. C.; Turner, G. M.; Schmittenmaer, C. A. Terahertz Spectroscopy. *J. Phys. Chem. B* **2002**, *106*, 7146–7159.

(23) Kužel, P.; Kadlec, F.; Němec, H. Propagation of Terahertz Pulses in Photoexcited Media: Analytical theory for Layered Systems. *J. Chem. Phys.* **2007**, *127*, 024506.

(24) Němec, H.; Kadlec, F.; Kužel, P. Methodology of an Optical Pump-Terahertz Probe Experiment: An Analytical Frequency-Domain Approach. *J. Chem. Phys.* **2002**, *117*, 8454–8466.

(25) Cardona, M.; Harbeke, G. Optical Properties and Band Structure of Wurtzite-Type Crystals and Rutile. *Phys. Rev.* **1965**, *137*, 1467–1476.

(26) Hecht, F.; Pironneau, O. *FreeFem++*; Université Pierre et Marie Curie, Paris, 2007.

(27) Rychetský, I.; Klíč, A. Dielectric Response of Arbitrary-Shaped Clusters Studied by the Finite Element Method. *Ferroelectrics* **2012**, *427*, 143–147.

(28) Hendry, E.; Koeberg, M.; Pijpers, J.; Bonn, M. Reduction of Carrier Mobility in Semiconductors Caused by Charge–Charge Interactions. *Phys. Rev. B* **2007**, *75*, 233202.

(29) Garnett, J. C. M. Colours in Metal Glasses and in Metallic Films. *Philos. T. R. Soc., London* **1904**, *203*, 385–420.

(30) Jepsen, P. U.; Fischer, B. M.; Thoman, A.; Helm, H.; Suh, J. Y.; Lopez, R.; Haglund, R. F. Metal-Insulator Phase Transition in a VO₂ Thin Film Observed with Terahertz Spectroscopy. *Phys. Rev. B* **2006**, *74*, 205103.

(31) The linear relationship means that the complex value ϵ_{eff} is proportional to the complex value ϵ_{int} (not to be confused with the statement that $\text{Re } \epsilon_{\text{eff}}$ and $\text{Im } \epsilon_{\text{eff}}$ is proportional to $\text{Re } \epsilon_{\text{int}}$ and $\text{Im } \epsilon_{\text{int}}$ respectively). Since the exact relation $\epsilon_{\text{eff}}(\epsilon_{\text{int}})$ contains also higher-order terms and since the first-order term vanishes for $\text{Re } \epsilon_{\text{eff}}$ we observe the second-order term in $\text{Re } \epsilon_{\text{eff}}$ which scales quadratically with $\text{Im } \epsilon_{\text{eff}}$.

(32) Nienhuys, H.-K.; Sundström, V. Influence of Plasmons on Terahertz Conductivity Measurements. *Appl. Phys. Lett.* **2005**, *87*, 012101.

(33) Rønne, C.; Åstrand, P.-O.; Keiding, S. R. THz Spectroscopy of Liquid H₂O and D₂O. *Phys. Rev. Lett.* **1999**, *82*, 2888–2891.

NOTE ADDED AFTER ASAP PUBLICATION

This article was published ASAP on December 23, 2013. Figures 3 and 4 have been modified. The correct version was published on December 30, 2013.